Nano Research
2022, 15(5): 4490–4499
ISSN 1998-0124 CN 11-5974/O4
https://doi.org/10.1007/s12274-021-3505-x

Birefringent response of graphene oxide film structurized via femtosecond laser

Tingting Zou[1,2], Bo Zhao[4], Wei Xin[1,3] (✉), Feiyue Wang[1,2], Hongbo Xie[1,2], Yuhang Li[1,2], Yuwei Shan[1], Kun Li[5], Yanbing Sun[5], and Jianjun Yang[1] (✉)

[1] *The GPL Photonics Laboratory, State Key Laboratory of Applied Optics, Changchun Institute of Optics, Fine Mechanics and Physics, Chinese Academy of Sciences, Changchun 130033, China*
[2] *Center of Materials Science and Optoelectronics Engineering, University of Chinese Academy of Sciences, Beijing 100049, China*
[3] *Key Laboratory of UV-Emitting Materials and Technology, Ministry of Education, Northeast Normal University, Changchun 130024, China*
[4] *Department of Electronic Information and Physics, Changzhi University, Changzhi 046011, China*
[5] *Changchun New Industries Optoelectronics Technology Co., Ltd, Changchun 130103, China*

Received: 9 January 2021 / **Revised:** 19 March 2021 / **Accepted:** 7 April 2021

ABSTRACT

In-plane birefringent materials present an effective modulation of the optical properties and more degrees of freedom for the signal detection in low dimension, and thus remain a hot topic in realizing the integrated, miniature, and flexible devices for multiple applications. Here, the artificial in-plane birefringence properties have been successfully achieved on a graphene oxide film by a novel femtosecond laser lithography method, which provides a high-speed, large-area, and regular subwavelength gratings (~ 380 nm) fabrication and photoreduction. The obtained sample manifests an evident optical birefringence (~ 0.18) and anisotropic photoresponse (~ 1.21) in the visible range, both of which can be significantly modulated by either the structural morphology or the degree of oxide reduction. Based on the analysis of effective-medium theory and measurements of angle-resolved polarized Raman spectroscopy, the artificial in-plane birefringence is originated from various optical responses of the periodic subwavelength structures for the incident light with different polarization states. This technique shows great advantages for the fabrication of integrated in-plane polarization-dependent devices, which is expected to solve the problems in this field, such as the deficient selection of materials, complex design of micro/nanostructure, and inflexible processing technology.

KEYWORDS

femtosecond laser lithography, reduced graphene oxide, subwavelength structures, in-plane birefringence, anisotropic photoresponse

1 Introduction

Recently, research into in-plane anisotropic photoelectric film materials has attracted much interest, especially in the field of polarization-dependent optoelectronics, microimaging, biological diagnosis, and military detection [1–3]. In contrast to the macro-spatial accumulation of optical path differences in traditional birefringent crystals (e.g. calcite and rutile), the anisotropic film materials can modulate the optical transmission and transport the light within a smaller space, which fills the bills of next-generation integrated devices. At present, typical anisotropic film materials can be divided into two types: natural two-dimensional van der Waals (2D-vdW) crystals and artificial metamaterial/surfaces or photonic crystals [4, 5]. In the former case, the anisotropic properties mainly depend on the in-plane asymmetrical crystal lattices. More than 20 kinds of anisotropic 2D materials have been discovered up to now, while most of them are prepared via mechanical exfoliation, which means that the large-scale preparation of them is difficult and their potential for practical applications are greatly restricted [6, 7]. Moreover, the anisotropic properties of 2D materials have proven to be closely related to its layer numbers, which creates the requirement of thickness uniformity during their fabrication [8]. In contrast, the properties of the latter material are mainly determined by the polarization-dependent coupling between the incident light and the periodic micro/nanostructures, which enables optical multiplexing and multifunction in a wide range of applications [9, 10]. In this case, despite the advantages of materials in photoelectric integration, the complex design of the structural units, the inflexibility, and the high costs of preparation remain the main obstacles to the practical applications of these metamaterials [10]. Therefore, it deserves to timely explore the artificial film material with excellent in-plane anisotropic photoelectric properties and to overcome the above-mentioned problems mainly in material selection and processing technology.

In this work, to achieve the above target, we propose a solution that combines a graphene oxide film (GO) with the femtosecond laser-induced periodic subwavelength grating structures on its surface. According to the effective-medium theory, the light propagation in such subwavelength grating structures is comparable to that in the homogeneous negative uniaxial birefringent crystals [11, 12]. However, the birefringence realized in the previous work is mainly focused on the bulk

---

Address correspondence to Wei Xin, xinwei@nenu.edu.cn; Jianjun Yang, jjyang@ciomp.ac.cn

materials [13–15], and thus being difficult to apply in integrated optoelectronics. In contrast, we successfully achieve the strong wide-band in-plane birefringent properties on a GO film with a thickness of less than 100 nm and an unprecedentedly small grating period of ~ 380 nm on the surface. Our design not only highlights the potential of materials in terms of the low dimension and excellent photoelectric properties, but also exhibits additional advantages with controlled flexibilities relating to the tunable laser parameters. By applying polarization-dependent optical transmission (T) spectroscopy and birefringence measurements, we determine a transmittance difference (ΔT), that is greater than 10% in the visible range (400–760 nm), and an in-plane birefringence as large as 0.18 at ~ 546 nm wavelength. Both measured values are comparable with those of existing natural (crystals and 2D materials) or artificial materials [13–18]. Furthermore, by measuring the angle-dependent photocurrent of our film, a strong anisotropic photoresponse (anisotropy ratio ~ 1.21) at the light wavelength of 532 nm is found. Through the modified theoretical analyses based on the effective-medium model and experimental measurements involving angle-resolved polarized Raman spectroscopy (ARPRS), we reveal that the above-mentioned birefringent phenomena originate from the discrepant optical modulations that are applied to the grating structures by the incident light with different polarizations [11, 12, 19, 20]. More delightfully, it is expected that the anisotropic properties of our artificial materials can be further improved via optimizing the structural parameters.

Here, a novel femtosecond laser lithography technology is adopted to produce the high-speed and large-area fabrication of the uniformly periodic subwavelength gratings on the GO film [21]. Compared with traditional processing methods, such as the nanoimprinting, electron-beam lithography, and self-assembly, femtosecond laser processing exhibits advantages in convenience, flexibility, efficiency, eco-friendliness, and low-cost operations [22–24]. Moreover, different from the common femtosecond laser processing methods, such as the direct writing and two-beam interference[25, 26], our fabrication technology shows superiorities in both processing efficiency and robustness due to the unique physical mechanisms, namely the excitation of TE surface wave (TE-SW). At the same time, as a result of the simultaneous laser-induced surface structure and oxide reduction processes on GO film, the GO material is gradually reduced with morphology change [27–29]. This process leads GO film to convert into structured reduced graphene oxide (S-rGO) material. When we tune the laser parameters (i.e. the overlapping pulse numbers and energy fluence), both the structure profile and the degree of oxide reduction (described via a complex refractive index, $\tilde{n} = n + i\kappa$) of the GO material can be effectively manipulated [21, 30]. This operation greatly simplifies the sample preparation, which is conducive to the subsequent research on the device. Specifically, to fabricate a centimeter-squared-sized (1 cm ×1 cm) surface sample with a spatial period of ~ 380 nm in our experiment will only require the time of about 2 min. This efficiency is improved more than four orders of magnitude when compared with the direct laser writing with the same parameters. By using a typical wet transfer method, we can transfer the S-rGO films from silicon onto other substrates (whether solid or flexible) while retaining its high quality [21]. Thus, all the above advantages, including the simple material selection, architecture design, and the convenient preparation of the samples, lay a solid foundation to expand this artificial in-plane photoelectric anisotropic material to practical applications in a wider space.

2 Results

2.1 Simultaneous microstructuring and oxide-reducing of GO films by femtosecond laser irradiation

Femtosecond lasers are proven to have the capabilities of morphological manipulation and photoreduction of GO materials, using the laser direct writing and the beam interference methods [25, 26, 28–30]. Femtosecond laser lithography, originated from the phenomena of laser-induced periodic surface structure (LIPSS), is deemed to possess a set of unique advantages of processing efficiency and robustness [31, 32]. However, such a technique usually produces poor quality structures, which becomes a substantial obstacle to many practical applications, especially for surface photonics devices. Due to the long-term immaturity of technology [31, 33–35], its practical implementation has not seriously arisen until recently. In this work, by employing a modified femtosecond laser lithography, we realized the high-speed and large-area fabrication of regular subwavelength surface structures on a silicon-based GO film (92 nm, in Fig. S1 in the Electronic Material (ESM)). The sample was prepared by spin-coating the GO solution several times to accurately control the film thickness, and the light irradiation was delivered via a chirped-pulse-amplification of Ti: sapphire femtosecond laser system (Spitfire Ace, Spectra Physics, 800 nm, 40 fs, 1 kHz). The incident laser intensity was expediently controlled by a combination of a half-wave plate and a Glan–Taylor prism, a second half-wave plate laying out behind was used to tune the laser polarization state. Following this, a frequency doubling crystal (Beta Barium Orate, BBO) was inserted to change the infrared light into the wavelength of λ = 400 nm, which was then focused by a cylindrical lens (with a 50 mm focal length) on the GO material at normal incidence. This produced a line-shaped focal spot with a large length-to-width ratio (namely, 10 mm/2.5 μm = 4,000). Such laser beam focusing is not only an essential prerequisite for the uniform distribution of the light intensity, but also a key strategy for improving the processing efficiency.

Figure 1(a) shows a schematic diagram of the femtosecond laser processing of GO film using our proposed strategy. When we precisely moved the sample, using the proper laser parameters, the highly uniform subwavelength grating structures were produced rapidly on the surface areas where the light was scanning. The structural orientation was strictly parallel to the direction of the light polarization, which provided a convenient way to regulate the structure arrangement when altering the laser polarization. In addition, influenced by the nonthermal or thermal photoreduction effects during the laser irradiation, the GO films were gradually reduced as well as morphologically processed, thus realizing the periodic microstructures on the reduced GO material [21]. A detailed description of the reduction of the GO film is presented in Fig. S2 in the ESM in which both micro-Raman spectroscopy (Horiba, Jobin Yvon) and X-ray photoelectron spectroscopy (XPS, Thermo Scientific K-Alpha) measurements were analyzed.

The morphologies of the S-rGO film were measured under a set of typical laser processing parameters, i.e. the laser fluence (F) was 49.1 mJ·m^{-2}, the scanning speed (v) was 40 μm·s^{-1} and the number of overlapping pulses in each laser spot (N_P) is 62. The thin film was characterized by both optical and scanning electron microscopy (SEM, Phenom), as shown in Figs. 1(b) and 1(c), respectively. Through examination of both the high-resolution morphology and the monochromatic green color of the structured surface (inset, 1 cm × 1 cm), we could ascertain that the high quality of the S-rGO film (without bending,

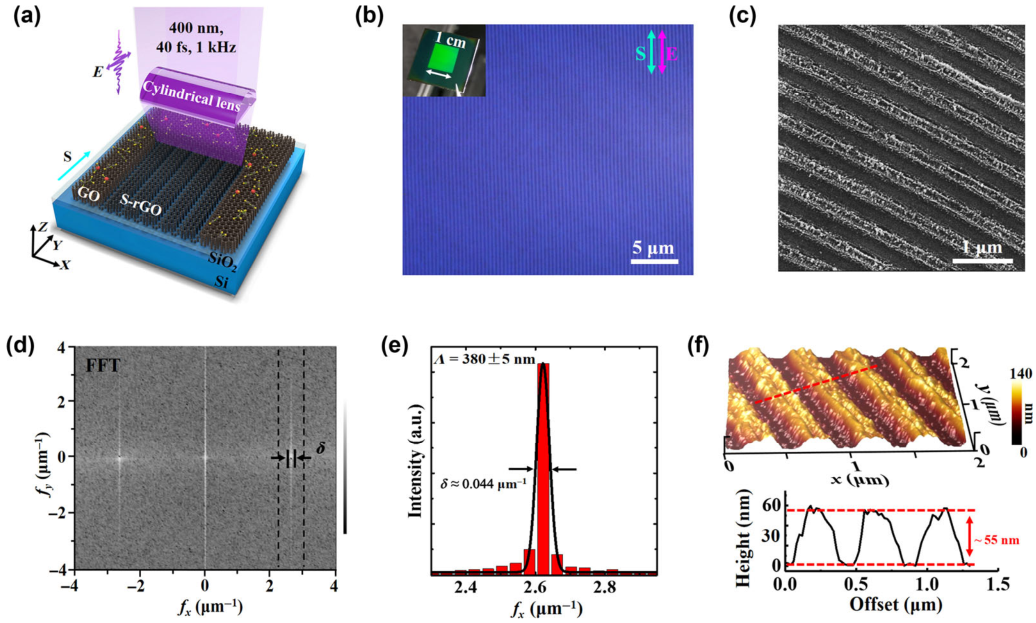

Figure 1 High-speed fabrication of the regular S-rGO films using femtosecond laser pulses. (a) Schematic diagram of the S-rGO formation via cylindrical focusing of the femtosecond laser irradiation. The periodic subwavelength gratings are generated on the laser-exposed large-area surface during the scanning process, and the surface areas without the laser illumination maintain the GO properties, indicating many oxygen-containing functional groups remain (the red and yellow spheres on the film). The cyan and purple arrows represent the directions of the laser scanning (S) and the linear polarization of the electric (E) field, respectively. (b) Optical images and (c) SEM images of the S-rGO. The homogenous green color of the image (inset) is the naked-eye observation of the whole S-rGO surface. (d) Calculated 2D-Fourier transformation (FFT) spectrum from the SEM image. (e) Derived intensity distribution of the spatial frequency for a distinct spot near the position of 2.62 μm^{-1} with a full-width-at-half-maximum (FWHM, δ) value of around 0.044 μm^{-1}, which corresponds to an average spatial period of Λ = 380±5 nm for the grating structures. (f) Measured 3D AFM image of the S-rGO, with a fluctuating height difference of around 55 nm.

bifurcation, and interruption) was produced with a uniform distribution even over a large area. A 2D fast FFT spectrum was then determined to further confirm the arrangement regularity of the laser-induced structures, as shown in Fig. 1(d). The available spatial frequencies are seen to mostly distribute near the position of f_x = 2.62 μm^{-1}, with a FWHM intensity value at δ = ~ 0.044 μm^{-1}. Such a narrow-range frequency distribution suggests a high uniformity for the subwavelength grating structures, which corresponds to an unprecedented period value of Λ = 380 ± 5 nm (Fig. 1(e)). Figure 1(f) shows a three-dimensional (3D) morphology of S-rGO film, which is provided from an atomic force microscopy (AFM, Bruker, Billerica). The height difference between the top and the valley of the grating structures is ~ 55 nm, which indicates no damage to the silicon substrate during the laser processing.

2.2 Formation mechanisms and dynamic morphology regulation of S-rGO films

When using our femtosecond laser lithography to prepare the S-rGO samples, two unique advantages are found. The first one is the vast potential for efficient processing: A key factor for determining the efficiency, while ensuring the processing quality, is the laser scanning speed, which can be varied over a range, reaching an upper limit of v = 80 μm·s^{-1}. Accordingly, the time required for processing a surface area of 1 cm × 1 cm into S-rGO with a period of 380 nm was shortened to ~ 125 s, which was about 4 orders of magnitude higher than the direct laser writing technique. This superiority is due to the interference mechanism of our femtosecond laser technology [21]. In brief, the incident Gaussian laser energy distribution is likely to be modified into the periodic strong-and-weak intensity fringes, when considering surface wave excitation and its interfering with the light, which ultimately results in the space-selective ablation and oxide reduction of the GO material surface [33–36]. Therefore, when the laser irradiates over the GO film, the periodic distribution of the micro/nanostructures begins to appear within the scanning area, which contrasts to the conventional micro-ablation pit phenomenon that arises from strong laser intensity. Moreover, from the observed grating orientation parallel to the polarization direction of the incident light, we can reasonably deduce the physical roles of TE surface wave (TE-SW) excitation. According to our previous report, when the GO film is irradiated by the femtosecond laser pulses, its optical permittivity (ε) began to gradient change from the surface towards the interior regions, accompanied with different levels of oxide reduction [21]. Such an inhomogeneous distribution of these optical properties contributes to the TE-SW excitation [37, 38], thus leading to the beginnings of the periodic grating structures on the sample surface (Fig. 2(a)). As the laser is focused onto the GO surface, the material ablation will lead to surface roughness, which seems to increase with the larger laser energy and pulse accumulation. As a result, the incident light can be certainly scattered by the roughened surface to result in a wave vector located within the sample surface [39], which subsequently interferes with the TE-SW to promote the grating structure formation. Upon successive irradiation of the femtosecond laser pulses, the initial periodic structures play an active role in the coupling of the light with the increased TE-SW energy. This positive feedback between the buildup of the period surface structures and the generated TE-SW energy is shown by the simulations of Fig. 2(b). Through examining the spatial profile of the calculated E field distribution along the z-direction, we determine that the maximum field intensity occurs close to the rGO-air interface (Fig. 2(c)). The detailed discussion of the TE-SW formation is discussed in Note S1, and Figs. S11 and S12 in the ESM.

In addition to its high efficiency, the femtosecond laser lithography technology has also shown exceptional robustness in microprocessing due to its nonlinear optical effects [31]. This enables the production of the high-quality periodic subwavelength

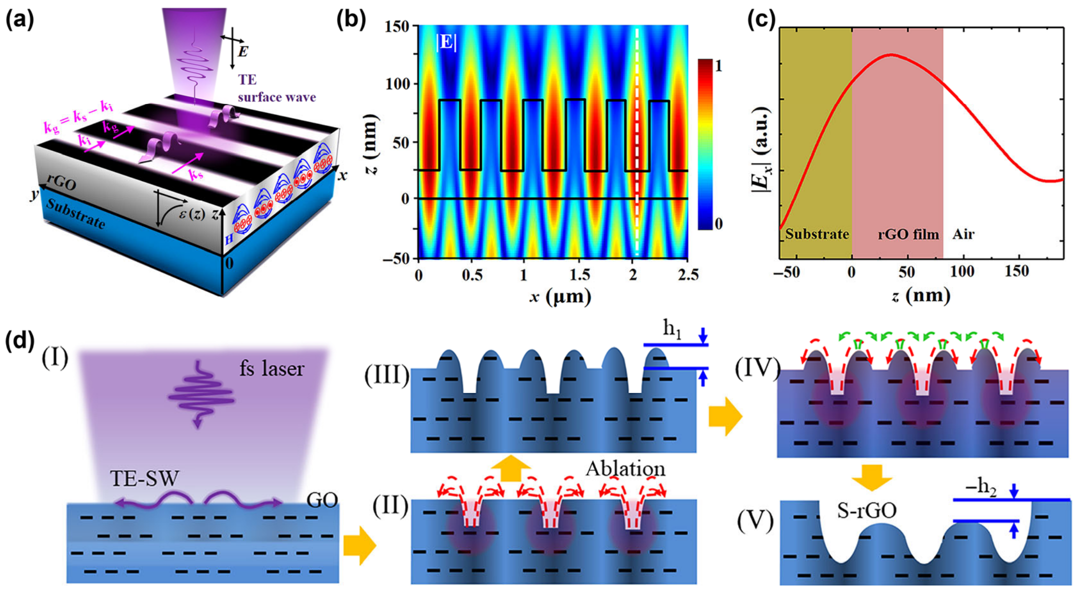

Figure 2 Physical mechanisms and dynamic regulation of the S-rGO. (a) Schematic of the theoretical model for the S-rGO formation. The grating vector of the structures is denoted by k_g. Both the vectors of incident light and the excited TE-mode surface wave are denoted by k_i and k_s, respectively. (b) Simulated resonant intensity fringes of the E field distribution on the sample surface, which are attained from a FDTD solution. The grating parameters are selected according to the measured morphology of the S-rGO film here. The overall thickness of the sample film is 80 nm with the etched groove depth and period as 55 and 380 nm, respectively. (c) Simulated variation trend of the *E* field intensity distribution along the *z*-direction (the white line in Fig. 2(b)). (d) Dynamical change of the morphology of the S-rGO film when increasing *F* or N_P.

surface structures within a large range of laser parameters. The suitable *F* and N_P values are in the range $F = \sim 16.4–56.3$ mJ·cm^{-2} and $N_P = \sim 40–5{,}000$, respectively (Fig. S3 in the ESM). The morphology of the S-rGO film can also be regulated dynamically in both depth and width by varying the laser parameters, which was characterized by the AFM images and shown in Fig. S4 in the ESM. By analyzing the morphology change of the sample surface in detail, the growing process of the S-rGO film is roughly shown in Fig. 2(d).

As mentioned previously, due to the interference between the incident light and TE-SW, the spatially periodic energy fringes are induced onto the GO film surface (Fig. 2(d) I). With an increase of *F* or N_P, the surface locations that correspond to the constructive interference fringes are at first ablated by the higher intensities (compared with the surface locations related to the destructive interference fringes), which make the oxygen-containing functional groups and part of the material remove. These are represented by the material spallation and the deposition of debris onto nearby surface regions (Fig. 2(d) II). On subsequent laser irradiation, the deposition of the spalled material tends to increase the thickness of S-rGO film (Fig. 2(d) III). Afterwards, when the laser parameters *F* or N_P increased further, the surface material within the beam spot is removed without any spatial selections due to the laser intensity exceeding the ablation threshold. This consequently decreases the overall thickness of the S-rGO film and prevents material depositions at the locations of the interference fringes (Figs. 2(d) IV and V). This type of femtosecond laser processing, thus, indicates the ability of flexible control of the surface morphology with varying the laser parameters, and is beneficial to further study of the optical properties that are triggered by the material structures.

2.3 In-plane birefringence effects of the S-rGO films

After the femtosecond laser processing, the S-rGO film can be transferred onto a transparent SiO_2 substrate for further investigation of its optical properties [21]. Figure 3(b) shows the measured polarization-dependent transmission spectra (Agilent, Cary 7000) in the visible wavelength range of 400–760 nm. When the incident light is linearly polarized perpendicular to the grating orientation, it is apparent that the corresponding optical transmission ($T_\perp$) of the structured sample is relatively higher than that ($T_{//}$) of the light polarization parallel to the grating orientation. The average difference between the two transmittances ($\Delta T = T_\perp - T_{//}$) is around 10%, with a maximum value of ~ 18% when the input wavelength is close to 543 nm, which suggests a strong optical birefringence effect. Usually, this type of phenomenon for the periodical subwavelength structures can be understood by the effective-medium theory [11, 12], as shown by a schematic shown in Fig. 3(a), the parameters *a* and *Λ* are the ridge width and the period of the grating, respectively.

The two effective refractive indices of the material, which correspond to the parallel and perpendicular directions relative to the grating orientation, respectively, are described by the following equations [11]:

$$n_{\parallel} = \sqrt{qn_1^2 + (1-q)n_2^2} \tag{1}$$

$$n_{\perp} = \sqrt{n_1 n_2 / \left[qn_2^2 + (1-q)n_1^2\right]} \tag{2}$$

where the parameter $q = a/\Lambda$ denotes the filling factor, and n_1, n_2 are the refractive constants of the materials that are periodically alternated. The indices $n_{//}$ and $n_\perp$ correspond to the slow and fast axes of the birefringent material, respectively.

The above theoretical model, however, only accounts for the real part of the complex refractive index ($\tilde{n}$), and the imaginary parts that mainly dominate the light absorption are neglected. To complement the theoretical model, it is necessary to obtain the complex index of the material through experiments, which will assist in the understanding of the photoelectric properties of the artificial material. To obtain the complex index of the subwavelength structured material, we experimentally measured the phase retardance ($\Delta\Phi$) of the sample films by using a birefringence microscope (CRi Abrio imaging system). Here, a filtered circularly polarized light beam with the wavelength of 546 nm illuminates the target at normal incidence, and a pair of liquid crystal retarders are positioned behind the sample to compensate for the phase difference. By analyzing

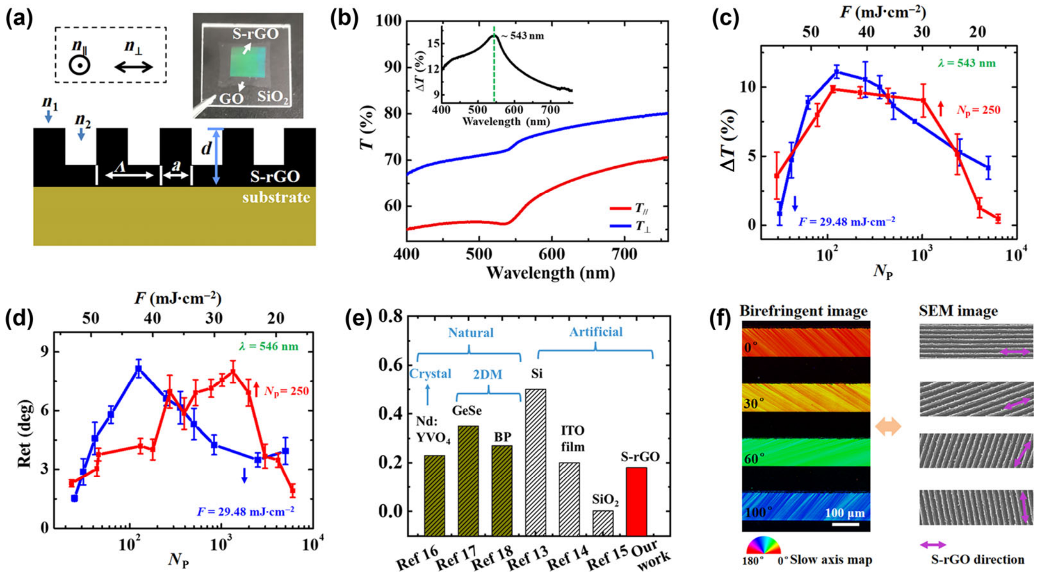

Figure 3 In-plane optical birefringence of the S-rGO films. (a) Schematic for the effective-medium model (main) and photo picture (inset) of a silica-based S-rGO sample. (b) Measured optical transmittances (T) of the S-rGO sample for illumination with two different linear polarization states (main) and their transmittance difference ($\Delta T = T_{//} - T_{\perp}$, inset) in the visible range, where the maximum difference of the spectral transmittance appears at around 543 nm. (c) Measured transmittance difference and (d) phase retardance of the S-rGO samples when varying the femtosecond laser parameters. Due to the characterizations with different systems, the corresponding wavelengths of the light illumination are slightly different. (e) Comparison of the optical birefringence of our S-rGO sample with several other reported materials. (f) SEM images (right) and the corresponding pseudo-color images of the phase retardance (left) for different S-rGO film samples. The slow optical axis of the material is always parallel to the orientation of the grating structure.

the resultant optical intensities obtained via a charge coupled device (CCD), which usually generates pseudo-color images [40], the in-plane phase retardance is determined at around $\Delta\Phi = \Phi_{//} - \Phi_{\perp} = 9.4°$ for the S-rGO film. The detailed optical path setting and measurement process can be found in Note S2 and Fig. S13 in the ESM. From the measured ΔT and $\Delta\Phi$ values, $\tilde{n}$ of the sample film can be obtained from the Kramers–Kronig relationship [19]. Consequently, both Δn and $\Delta\kappa$ for the S-rGO films can be attained, the details on which are found in Note S3 in the ESM.

We then measured the variation trends of ΔT for the periodically subwavelength S-rGO film with different laser processing parameters, such as F (over the range 17.4–56.2 mJ·cm^{-2}) and N_P (50–5,000), as shown in Fig. 3(c). The measured variations of $\Delta\Phi$ as a function of F and N_P are shown in Fig. 3(d), which demonstrates the flexible performance of the modulation of our samples when using the femtosecond laser pulses. Furthermore, we converted the measurement of phase retardance into the real part of the difference of the refractive index ($\Delta n = |n_{//} - n_{\perp}|$) with the formula $\Delta n = \Delta\Phi / (d \times k) = \sim 0.18$, where d is the thickness of the rGO film and $k = 2\pi/\lambda$ is the wave vector in a vacuum. A comparison of Δn of our sample with other reported materials is shown in Fig. 3(e) and Table S1 in the ESM, this indicates that the optical birefringence of the S-rGO film is competitive. In addition, similar to the birefringent properties of other subwavelength grating structures, the optical slow-axis of our film is also found parallel to the grating direction [11–15]. This is clearly seen in the pseudo-color images that are obtained from our microscope system (Fig. 3(f)). Based on the Kramers–Kronig relations, the high performance and flexible regulation in birefringence properties of our samples are related to the complex refractive index, which lays a foundation for the full understanding of the photoelectric property of the artificial materials.

2.4 Verification of mechanisms for the birefringence of S-rGO films

GO is an isotropic material with the symmetrical lattice structure. In the above analysis, we only considered the complex refractive index induced by the grating structure on birefringence formation. However, the birefringence response may be also affected if the lattice of GO changes into asymmetric after femtosecond laser striking. To rectify this issue, an ARPRS with an excitation wavelength of 532 nm (Horiba, Jobin Yvon), which is a widely employed method for determining the electron-photon–phonon interactions, crystalline orientation, and vdW interlayer coupling, was used to analyze the lattice and phonon symmetry of our S-rGO materials [20, 41, 42]. Here, the polarization states of both the incident and the scattered lights were fixed parallel to each other, and the grating structure orientation was initially parallel to the light polarization direction. We rotated the sample (S-rGO/SiO$_2$/Si) counterclockwise by steps of 15° and then recorded the polarization-dependent Raman intensity for each step. The measurement set up is shown in Fig. S5 in the ESM. According to the Placzek approximation, the Raman scattering intensity was calculated from $|\hat{e}_l \cdot \hat{R} \cdot \hat{e}_s|^2$, where $\hat{R}$ is the Raman tensor of the material corresponding to the Raman mode and $\hat{\boldsymbol{e}}_l$ and $\hat{e}_s$ represent the polarization vectors of the incident and scattered lights, respectively [20]. For the anisotropic 2D materials with asymmetric lattice, some Raman peaks show active Raman modes, and the corresponding $\hat{R}$ will lead the angle-dependence Raman scattering intensities. But for the isotropic material, there are no active Raman modes in Raman peaks, which means the $\hat{R}$ in these isotropic materials cannot induce angle-dependent Raman intensities.

For the GO or rGO films, their Raman spectra generally display three characteristic peaks, namely the D peak at ~ 1,360 cm^{-1}, G peak at ~ 1,680 cm^{-1}, and 2D peak at ~ 2,690 cm^{-1} [43]. The G peak represents the E_{2g} vibration mode of the ordered sp^2 bond structure of carbon materials, while the D peak corresponds to the defect or the amorphous structures. Figure 4(a) shows the ARPRS map of our samples. When the angular position of the sample is rotated from 0° to 360°, it is determined that the polarization-dependent Raman intensity changes periodically, with the largest values at 90° or 270° while the

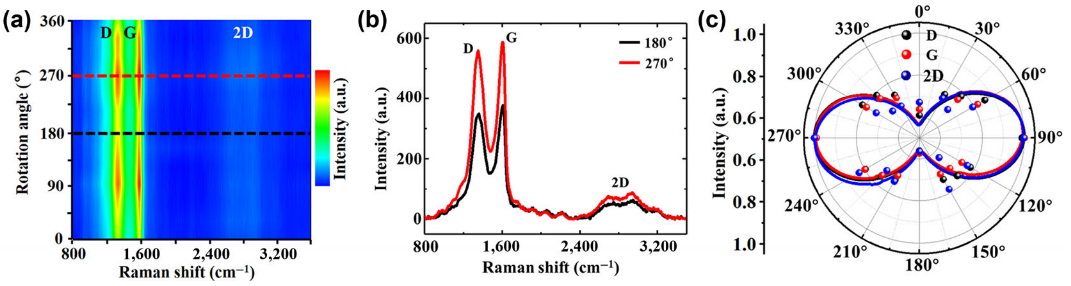

Figure 4 Measured ARPRS for the S-rGO films. (a) Polarization-dependent Raman map of the samples. Three typical characteristic peaks (D, G, and 2D) of the carbon materials are observed. The rotation angle represents the counter-clockwise movement of the structure orientation with respect to the light polarization direction. (b) Raman spectra of the sample, when the rotation angles are fixed at 180° and 270°, corresponding to the positions marked as black and red dotted lines in the Raman map of Fig. 4 (a), respectively. (c) Polarization-dependent Raman intensities of D, G, and 2D peaks of the S-rGO sample after normalization, they clearly show the same variation trend.

weakest at 0° (360°) or 180°, as shown in Fig. 4(b). This phenomenon is similar to the properties of common anisotropic 2D materials, but the main difference is that the variation trend of each peak value of our sample is highly consistent (Fig. 4(c)). The polarization states of the incident and scattered lights, corresponding to the vectors $\hat{e}_l$ and $\hat{e}_s$ respectively, have no change during the experiment. This interesting phenomenon means that the forms of the tensor $\hat{R}$ are identical for the three different Raman modes, and there is no lattice change in the GO material after laser structuring.

However, the reason of the observed same variation anisotropic tendency for three Raman peaks in our sample still needs to be identified. In order to understand this phenomenon, we employed FDTD solutions to simulate the localized field distribution on S-rGO surface irradiated by 532 nm laser with different polarizations (Fig. S6 in the ESM). It is shown that the localized field intensity on S-rGO film is much higher for the light polarization perpendicular to the grating orientation than that of other parallel situations. The localized field with different polarizations may cause the polarized light absorption and reflection. We further used the polarization-dependent reflection measurement to verify this deduction. The details on these reflection results are given in Fig. S7 in the ESM. As a result, a similar variation tendency is indeed observed. These results confirm that the variation of three Raman peaks originate from the grating structure rather than its intrinsic lattice properties. From another perspective, these phenomena indicate that the birefringence in our sample is due to grating structures induced the different effective refractive index between $n_{//}$ and $n_{\perp}$ arising from the subwavelength grating structures on the surface, rather than the change in the vibration mode of the lattice.

2.5 In-plane photoelectric anisotropy of S-rGO films

The optical anisotropy exhibited by our films is derived from the birefringent $\tilde{n}$ of the material. Since the difference in Δk of $\tilde{n}$ is related to the light absorption of the material, its in-plane anisotropic absorption and the photoresponse of our sample can be determined [21]. In order to verify this deduction, we first experimentally measure T and reflection (R) of the film sample and calculated the light absorption behavior with the formula $A = 1 - T - R$, whose variations within a wide range are shown in Fig. S8 in the ESM. We find that the absorption of the structured films for the light polarization parallel to the grating orientation ($A_{//}$) is always larger than that of the perpendicular situation ($A_{\perp}$). The maximum difference ($\Delta A = A_{//} - A_{\perp}$) of ~ 18% is observed at the wavelength ~ 540 nm. The detailed experimental results are presented in Fig. S8 in the ESM and Fig. 5(b). Furthermore, we deposited the square gold electrodes arrays (50 nm in dimensions) on our sample surface to design an in-plane anisotropic photodetector (Au/S-rGO/SiO_2). As shown in Fig. 5(a), α is defined as the angle between the current flow direction and the grating orientation. The electrodes connection methods can be selected as $\alpha = 0°$ or $\alpha = 90°$. A continuous-wave laser with a wavelength of 532 nm was selected as the optical exciter for the device, and the laser spot diameter is about 100 μm after focusing by a 4 × objective lens. The direction of its linear polarization was controlled by rotating a half-wave plate. Before measuring the photoelectronic response, the anisotropic electron transport properties under two electrodes connection methods were obtained (Fig. S9 in the ESM). The results show that the electronic transportation in $\alpha = 0°$ situation is always larger than its counterpart. To make measurements of the anisotropic photoresponse clearly and distinguishable, we chose adjacent electrodes in $\alpha = 0°$ as the source and drain for the next following anisotropic photoelectronic response measurement, which enables the highest conductivity.

The angle between the incident light polarization and grating orientation is defined as β, by rotating the half-wave plate to change the value of β every 30°, the corresponding photocurrents were obtained. The left image in Fig. 5(b) shows the results for the polarization-dependent photoresponse when the incident light power (P) and the source-drain voltage (V_{sd}) are fixed as 50 mW and 5 V, respectively. Similar to the properties of other anisotropic 2D materials, the photoresponse of our sample also changes with different light polarizations [6]. When the polarization direction of the light becomes parallel ($\beta = 0°$) and vertical ($\beta = 90°$) to the grating, the measured photocurrent (PC) can reach maximum (PC_{Max}) and minimum (PC_{Min}) values, respectively. $PC = I_{light} - I_{dark}$, where I_{light} is the measured current when light is on, I_{dark} is the measured current without light irradiation. A ratio of $\sigma_{PC} = PC_{Max}/PC_{Min}$ is defined to represent the polarized performance of the device. The larger value means the better polarized performance. The typical value $\sigma_{PC} = 1.16$ is obtained in the left image of Fig. 5(b). Noticeably, the variation in the measured PC value is consistent with the polarization-dependent light absorption of our material, which is shown by the right image of Fig. 5(b). In addition, the normalized optical-switching experiment in Fig. 5(c) shows the stable polarized performance. The observations show an interesting phenomenon with either the rise or the fall time (t_r, t_f) of 70 ms and 180 ms, respectively, near an order of magnitude faster than those given in other reports [21, 44]. This may be due to the relatively insignificant thermal effect in our subwavelength grating structures. Then, we measured the polarization-dependent PC_{Max} and PC_{Min} when increasing P of the light from 5 to 150 mW, and the corresponding polarized photoresponsivity (R) is obtained in Fig. 5(d), while R can be calculated as: $R = PC / (P \times (S_d/S_l))$,

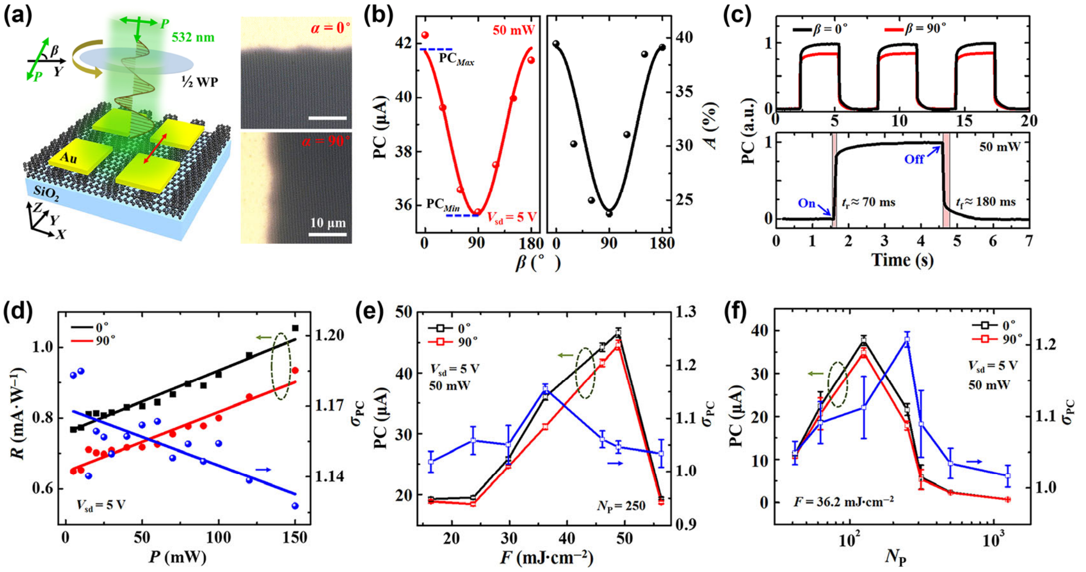

Figure 5 Polarization-dependent photoresponse of the S-rGO devices. (a) The schematic and the photographic images of our in-plane photoelectric anisotropic device. Electrode connection at $\alpha = 0°$ (red arrow) is applied for the PC measurement, and a half-wave plate (1/2 WP) is used for changing β. All the scale bars are 10 μm. (b) Measured polarization-dependent photocurrent (PC, left) and its corresponding absorption (right) of the S-rGO film device. c) Normalized photocurrent as a function of time with a power of 50 mW for the light illumination, in which the rise and fall times are $t_r = 70$ ms and $t_f = 180$ ms, respectively. (d) Variation of the R and σ_{PC}, while gradually increasing the illumination intensity from 5 to 150 mW. (e) and (f) Measured polarization-dependent PC and σ_{PC} of our samples that are processed with different laser parameters. The overlapping pulses in each laser spot are initially fixed at $N_P = 250$, and the incident laser fluence changes from 16.4 to 56.3 mJ·cm^{-2}. Then, on fixing F to 36.2 mJ·cm^{-2}, the pulse number changes from 40 to 1,250.

where S_l is laser spot area and S_d is the effective device area. As the P gradually increases, the anisotropy σ_{PC} is also obtained in Fig. 5(d). It slightly decreases from 1.18 to 1.12 as shown in Fig. 5(d), which indicates the incident light power has a little influence on the σ_{PC}. Also, the measured PC values appear to increase with the power of the incident light. They are clearly distinguishable from the dark current shown in Fig. S10 in the ESM. The larger the gap between the PC and the dark current, the more favorable the discussed optoelectronic device becomes.

A detailed study of the anisotropic photoresponses of our devices was conducted further. Since the anisotropy strongly depends on the morphology and the degree of reduction of the S-rGO samples, we can modify the properties of the materials by changing the parameters of the femtosecond laser processing. Regulation of the anisotropy photoresponses within our devices is thus possible. Here, our main concern is the incident laser fluence (F) and the number of overlapping pulses (N_P) within the spot. On the premise of ensuring the formation of the rGO structure, one final laser parameter is varied over a wide range (while fixing the other parameters) to produce samples with different photoelectrical characteristics. Figures 5(e) and 5(f) show the measured polarization-dependent photocurrents and σ_{PC} for different cases, each PC was obtained by measuring three times on three pairs adjacent electrodes and calculating the average and standard value, and the corresponding σ_{PC} was calculated. It is clearly that the value of σ_{PC} can be modulated in a relative large range (~ 1.02–1.21) as F and N_P vary. The flexible modulation of σ_{PC} indicates that our artificial S-rGO devices have major advantages over most natural anisotropic materials [6].

3 Discussion

The artificial in-plane anisotropic 2D materials potentially have a broad range of practical applications, because their physical properties can be effectively controlled at a low dimension to overcome the shortcomings of traditional materials for on-chip integration. The main highlights of this work focus on the proper selection of materials, the micro/nano-structure design of the surface, and the high-speed laser processing. In general, rGO material with excellent photoelectric properties is a competitive candidate to be applied in the relevant research field because they meet the requirements of large-scale and high-quality industrial usage [45]. However, there are still some problems to face in their structure design and process. Firstly, the integrated photonic elements may require the desirable property that the featured material sizes are smaller than the working light wavelength and they also need to be arranged periodically over a large area. Secondly, to facilitate their fabrication, the morphologies of the micro/nanostructures are expected to be as simple as possible. These issues may indeed hinder the practical applications of the existing research [10]. Our work aims to effectively solve these problems by using TE-SW based femtosecond laser lithography to fabricate large-area are high-quality S-rGO films. Combined with our previous work, this technique can be further optimized for the higher-resolution structured rGO by applying the shorter wavelength of the incident laser [21].

Our technology is a novel processing method, especially suitable for the periodic micro/nanostructuring of material surfaces [46, 47]. Since plenty of work showed that the material with subwavelength gratings could act as a birefringent crystal, it is reasonable to believe that our design can realize the in-plane anisotropic control of the material's photoelectric properties. [13–15] The subsequent photoelectric measurements have obviously confirmed the idea. However, the anisotropic performance of our samples may not be seen as excepted, like the lower photoresponse ratio compared with existing natural materials (Table S2 in the ESM), which still need further optimization. According to effective-medium theory, the anisotropy of materials mainly depends on the spatial regularity and the periodic alternating refractive index (n_1 and n_2) in the structure [13–15]. If the periodic structures are well-organized, the light experiences a lower number of unnecessary scattering events when passing through the material, thus the efficiency of the birefringent and photoresponse ratio can be improved.

Due to the unique physical mechanisms that underpin our sample, our technology possesses an intrinsic advantage in its processing quality and robustness. When the refractive index difference ($|n_1 - n_2|$) of the adjacent media in the periodic structures increases, the birefringent effect will be enhanced. Since the refractive index of the GO material is inclined to change (0.6–0.8) during its oxide reduction process, it also presents a huge competitive advantage over most conventional materials (0.2–0.4) [30, 48]. In addition, the grating structure can form on GO films with different thickness, and its period can be effective manipulated by modulating laser wavelength [21]. Optimizing these parameters may also improve the anisotropic performance. Briefly, the birefringent and anisotropic photoelectronic performance of the device are possible to be further improved by optimizing the laser processing parameters and reasonable structural design.

4 Conclusions

In summary, an artificial in-plane optical birefringence and anisotropic photoelectric properties on a S-rGO film are achieved by adopting a novel femtosecond laser lithography technology to prepare large-area subwavelength periodic grating surface structures, as well as an *in-situ* oxide reduction process. Such a regular small period of 380 nm and the high robustness of the structure formation are originated from the excitation of the TE-mode surface wave. An optical birefringence value of $\Delta n = 0.18$ and an anisotropic photoresponse ratio of $\sigma_{PC} = 1.21$ are obtained in the visible range, and both properties can be further optimized by tuning the structures morphology and degree of oxide reduction. A comprehensive understanding of the birefringent properties is based on the effective-medium model and the measurements involving ARPRS. The selective restriction of the transmission of incident light with different polarization states in the subwavelength gratings obviously plays a key role. In general, this work provides a convenient and feasible model for the fabrication of artificial in-plane birefringent materials, especially in the choice of material selection, structural design, and high-speed processing, which can open perspectives for the novel device production and applications in practice.

5 Methods

5.1 Preparation of S-rGO based optical and photoelectric devices

Firstly, the GO powders prepared by the modified Hummer method were dissolved in deionized water at a concentration of 4 mg·mL^{-1} for 1 h with the help of ultrasonic wave to make GO solution. By spin coating the solution several times on a silicon substrate (Si/SiO$_2$, 300 nm) at 2,500 rpm for 30 s, a GO film with a thickness about 92 nm was prepared. When this coating was repeated several times, the thickness of GO film could reach the requirement for laser processing. The femtosecond laser irradiation was delivered from a commercial Ti: sapphire femtosecond laser amplifier system (Spitfire Ace, Spectra Physics, 800 nm, 40 fs, and 1 kHz). In particular, a BBO crystal was used in the optical path to change the central wavelength of the output infrared laser pulses into $\lambda = 400$ nm, and a cylindrical lens was employed for generating a line-shaped focal beam spot. By changing the laser processing parameters, such as the energy fluence from 17.4 to 56.2 mJ·cm^{-2} and the scanning speed that causes the partially overlapping pulses in each laser spot from 50 to 5,000, a large area (centimeter scale) of the highly regular (380 nm period) S-rGO could be conveniently fabricated on the GO film surface. After that, by using the traditional wet transfer method, we could transfer the S-rGO film onto a silica substrate to build an in-plane anisotropic optical device. Moreover, if we deposited gold electrode pairs (50 nm thickness) on its surface, an anisotropic photoelectric device was made. The width of the square electrode was 500 μm, and each two adjacent square electrodes space was 50 μm.

5.2 Characterizations

S-rGO samples were optically imaged by a laser microscope (Keyence, VK-X1000), and their detailed surface morphologies were characterized by AFM (Bruker, Billerica) and SEM (Phenom, Eindhoven). The spatial period of the laser-induced structures and the standard deviation was calculated by 2D-FFT of SEM images with the help of the MATLAB software. The emergence of rGO after the laser treatment was investigated by a Raman spectrometer (LabRAM HR evolution), and its showing optical retardance was observed by a birefringence microscope (CRi Abrio imaging system). The experiment of polarization-dependent light absorption for the S-rGO samples was measured by a UV–vis-NIR spectrometer (Agilent, Cary 7000), and their photoresponse were tested by a semiconductor analyzer (Keithley, 4200A). A continuous-wave light with a wavelength of 532 nm (MGL-II-532, CNI) was used for photo detection.

5.3 Theoretical simulation

The simulation for the formation mechanisms of S-rGO was carried out by a software (Lumerical FDTD solutions software package), in which the thickness of rGO film sample was set as 80 nm with the grating period of 380 nm, and both the width and depth of the gratings were 200 and 55 nm, respectively. The incident light source was a Gaussian profiled plane wave of TE-polarization at the wavelength of 400 nm. The boundary in the z-direction was a perfectly matched layer, while the x-y-direction boundaries were satisfied with the periodic conditions. The real part of the refractive index and the corresponding z-dependent dielectric constant of rGO material was quoted in the literature [21].

Acknowledgements

The research is financially supported by the K. C. Wong Education Foundation (No. GJTD-2018-08), the National Natural Science Foundation of China (Nos. 91750205, 11674178, and 11804334), and the Jilin Provincial Science & Technology Development Project (No. 20180414019GH). The authors thank prof. Peter G. Kazansky and Dr. Yuhao Lei from the Optoelectronics Research Centre, University of Southampton for testing the optical birefringence properties of the samples.

Electronic Supplementary Material: Supplementary material (characterizations of GO film before and after laser irradiation; window conditions for the S-rGO formation; dynamically morphology regulation of the S-rGO; set up for birefringence, raman scattering and angle-resolved reflection measurement; anisotropic optical properties of S-rGO; simulated TE-SW generation on GO surface; and birefringence formation of S-rGO mechanism) is available in the online version of this article at https://doi.org/10.1007/s12274-021-3505-x.

References

[1] Rubin, N. A.; D'Aversa, G.; Chevalier, P.; Shi, Z. J.; Chen, W. T.; Capasso, F. Matrix Fourier optics enables a compact full-Stokes

polarization camera. *Science* **2019**, *365*, eaax1839.
[2] Tong, L.; Huang, X. Y.; Wang, P.; Ye, L.; Peng, M.; An, L. C.; Sun, Q. D.; Zhang, Y.; Yang, G. M.; Li, Z. et al. Stable mid-infrared polarization imaging based on quasi-2D tellurium at room temperature. *Nat. Commun*. **2020**, *11*, 2308.
[3] Vasefi, F.; MacKinnon, N.; Saager, R. B.; Durkin, A. J.; Chave, R.; Lindsley, E. H.; Farkas, D. L. Polarization-sensitive hyperspectral imaging *in vivo*: A multimode dermoscope for skin analysis. *Sci. Rep*. **2014**, *4*, 4924.
[4] Ma, W. L.; Alonso-González, P.; Li, S. J.; Nikitin, A. Y.; Yuan, J.; Martín-Sánchez, J.; Taboada-Gutiérrez, J.; Amenabar, I.; Li, P. N.; Vélez, S. et al. In-plane anisotropic and ultra-low-loss polaritons in a natural van der Waals crystal. *Nature* **2018**, *562*, 557–562.
[5] Nicholls, L. H.; Rodríguez-Fortuño, F. J.; Nasir, M. E.; Córdova-Castro, R. M.; Olivier, N.; Wurtz, G. A.; Zayats, A. V. Ultrafast synthesis and switching of light polarization in nonlinear anisotropic metamaterials. *Nat. Photonics* **2017**, *11*, 628–633.
[6] Li, L.; Han, W.; Pi, L. J.; Niu, P.; Han, J. B.; Wang, C. L.; Su, B.; Li, H. Q.; Xiong, J.; Bando, Y. et al. Emerging in-plane anisotropic two-dimensional materials. *InfoMat* **2019**, *1*, 54–73.
[7] Zhong, J. H.; Yu, J.; Cao, L. K.; Zeng, C.; Ding, J. N.; Cong, C. X.; Liu, Z. W.; Liu, Y. P. High-performance polarization-sensitive photodetector based on a few-layered $PdSe_2$ nanosheet. *Nano Res*. **2020**, *13*, 1780–1786.
[8] Wang, C.; Zhang, G. W.; Huang, S. Y.; Xie, Y. G.; Yan, H. G. The optical properties and plasmonics of anisotropic 2D materials. *Adv. Opt. Mater*. **2020**, *8*, 1900996.
[9] Chen, S. Q.; Liu, W. W.; Li, Z. C.; Cheng, H.; Tian, J. G. Metasurface-empowered optical multiplexing and multifunction. *Adv. Mater*. **2020**, *32*, 1805912.
[10] Soukoulis, C. M.; Wegener, M. Past achievements and future challenges in the development of three-dimensional photonic metamaterials. *Nat. Photonics*. **2011**, *5*, 523–530.
[11] Flanders, D. C. Submicrometer periodicity gratings as artificial anisotropic dielectrics. *Appl. Phys. Lett*. **1983**, *42*, 492–494.
[12] Kikuta, H.; Ohira, Y.; Iwata, K. Achromatic quarter-wave plates using the dispersion of form birefringence. *Appl. Opt*. **1997**, *36*, 1566–1572.
[13] Drevinskas, R.; Beresna, M.; Zhang, J. Y.; Kazanskii, A. G.; Kazansky, P. G. Ultrafast laser-induced metasurfaces for geometric phase manipulation. *Adv. Opt. Mater*. **2017**, *5*, 1600575.
[14] Cerkauskaite, A.; Drevinskas, R.; Solodar, A.; Abdulhalim, I.; Kazansky, P. G. Form-birefringence in ITO thin films engineered by ultrafast laser nanostructuring. *ACS Photonics* **2017**, *4*, 2944–2951.
[15] Sakakura, M.; Lei, Y. H.; Wang, L.; Yu, Y. H.; Kazansky, P. G. Ultralow-loss geometric phase and polarization shaping by ultrafast laser writing in silica glass. *Light: Sci. Appl*. **2020**, *9*, 15.
[16] MT-Optics. *YVO₄* [Online]. http://www.mt-optics.com/YVO4.html (accessed Dec 6, 2020).
[17] Yang, Y. S.; Liu, S. C.; Wang, Y.; Long, M. S.; Dai, C. M.; Chen, S. Y.; Zhang, B.; Sun, Z.; Sun, Z. Y.; Hu, C. G. et al. In-plane optical anisotropy of low-symmetry 2D GeSe. *Adv. Opt. Mater*. **2019**, *7*, 1801311.
[18] Lan, S. F.; Rodrigues, S.; Kang, L.; Cai, W. S. Visualizing optical phase anisotropy in black phosphorus. *ACS Photonics* **2016**, *3*, 1176–1181.
[19] Zheng, X. R.; Xu, B.; Li, S.; Lin, H.; Qiu, L.; Li, D.; Jia, B. H. Free-standing graphene oxide mid-infrared polarizers. *Nanoscale* **2020**, *12*, 11480–11488.
[20] Mao, N. N.; Zhang, S. Q.; Wu, J. X.; Zhang, J.; Tong, L. M. Lattice vibration and Raman scattering in anisotropic black phosphorus crystals. *Small Methods* **2018**, *2*, 1700409.
[21] Zou, T. T.; Zhao, B.; Xin, W.; Wang, Y.; Wang, B.; Zheng, X.; Xie, H. B.; Zhang, Z. Y.; Yang, J. J.; Guo, C. L. High-speed femtosecond laser plasmonic lithography and reduction of graphene oxide for anisotropic photoresponse. *Light*: *Sci*. *Appl*. **2020**, *9*, 69.
[22] Zhao, Y.; Belkin, M. A.; Alù, A. Twisted optical metamaterials for planarized ultrathin broadband circular polarizers. *Nat. Commun*. **2012**, *3*, 870.
[23] Chanda, D.; Shigeta, K.; Gupta, S.; Cain, T.; Carlson, A.; Mihi, A.; Baca, A. J.; Bogart, G. R.; Braun, P.; Rogers, J. A. Large-area flexible 3D optical negative index metamaterial formed by nanotransfer printing. Nat. *Nanotechnol*. **2011**, *6*, 402–407.
[24] Vignolini, S.; Yufa, N. A.; Cunha, P. S.; Guldin, S.; Rushkin, I.; Stefik, M.; Hur, K.; Wiesner, U.; Baumberg, J. J.; Steiner, U. A 3D optical metamaterial made by self-assembly. *Adv. Mater*. **2012**, *24*, OP23–OP27.
[25] Lin, H.; Sturmberg, B. C. P.; Lin, K. T.; Yang, Y. Y.; Zheng, X. R.; Chong, T. K.; de Sterke, C. M.; Jia, B. H. A 90-nm-thick graphene metamaterial for strong and extremely broadband absorption of unpolarized light. *Nat. Photonics* **2019**, *13*, 270–276.
[26] Jiang, H. B.; Zhang, Y. L.; Han, D. D.; Xia, H.; Feng, J.; Chen, Q. D.; Hong, Z. R.; Sun, H. B. Bioinspired fabrication of superhydrophobic graphene films by two-beam laser interference. *Adv. Funct. Mater*. **2014**, *24*, 4595–4602.
[27] Jiang, L.; Wang, A. D.; Li, B.; Cui, T. H.; Lu, Y. F. Electrons dynamics control by shaping femtosecond laser pulses in micro/nanofabrication: Modeling, method, measurement and application. *Light*: *Sci*. *Appl*. **2018**, *7*, 17134.
[28] Jiang, H. B.; Zhao, B.; Liu, Y.; Li, S. Y.; Liu, J.; Song, Y. Y.; Wang, D. D.; Xin, W.; Ren, L. Q. Review of photoreduction and synchronous patterning of graphene oxide toward advanced applications. *J. Mater. Sci*. **2020**, *55*, 480–497.
[29] You, R.; Liu, Y. Q.; Hao, Y. L.; Han, D. D.; Zhang, Y. L.; You, Z. Laser fabrication of graphene-based flexible electronics. *Adv. Mater*. **2020**, *32*, 1901981.
[30] Zheng, X. R.; Jia, B. H.; Lin, H.; Qiu, L.; Li, D.; Gu, M. Highly efficient and ultra-broadband graphene oxide ultrathin lenses with three-dimensional subwavelength focusing. *Nat. Commun*. **2015**, *6*, 8433.
[31] Öktem, B.; Pavlov, I.; Ilday, S.; Kalaycıoğlu, H.; Rybak, A.; Yavaş, S.; Erdoğan, M.; Ilday, F. Ö. Nonlinear laser lithography for indefinitely large-area nanostructuring with femtosecond pulses. *Nat. Photonics* **2013**, *7*, 897–901.
[32] Birnbaum, M. Semiconductor surface damage produced by ruby lasers. *J. Appl. Phys*. **1965**, *36*, 3688–3689.
[33] Bonse, J.; Höhm, S.; Kirner, S. V.; Rosenfeld, A.; Krüger, J. Laser-induced periodic surface structures–A scientific evergreen. *IEEE J. Sel. Top. Quant. Electron*. **2017**, *23*, 9000615.
[34] Huang, M.; Zhao, F. L.; Cheng, Y.; Xu, N. S.; Xu, Z. Z. Origin of laser-induced near-subwavelength ripples: Interference between surface plasmons and incident laser. *ACS Nano* **2009**, *3*, 4062–4070.
[35] Wang, L.; Chen, Q. D.; Cao, X. W.; Buividas, R.; Wang, X. W.; Juodkazis, S.; Sun, H. B. Plasmonic nano-printing: Large-area nanoscale energy deposition for efficient surface texturing. *Light*: *Sci*. *Appl*. **2017**, *6*, e17112.
[36] Chen, J. N.; Badioli, M.; Alonso-González, P.; Thongrattanasiri, S.; Huth, F.; Osmond, J.; Spasenović, M.; Centeno, A.; Pesquera, A.; Godignon, P. et al. Optical nano-imaging of gate-tunable graphene plasmons. *Nature* **2012**, *487*, 77–81.
[37] Shvartzburg, A.; Petite, G.; Auby, N. *S*-polarized surface electromagnetic waves in inhomogeneous media: Exactly solvable models. *J. Opt. Soc. Amer. B* **1999**, *16*, 966–970.
[38] Sun, Z. J.; Zuo, X. L.; Guan, T. P.; Chen, W. Artificial TE-mode surface waves at metal surfaces mimicking surface plasmons. *Opt. Express* **2014**, *22*, 4714–4722.
[39] Bonse, J.; Graf, S. Maxwell meets Marangoni–a review of theories on laser-induced periodic surface structures. *Laser Photonics Rev*. **2020**, *14*, 2000215.
[40] Shribak, M.; Oldenbourg, R. Techniques for fast and sensitive measurements of two-dimensional birefringence distributions. *Appl. Opt*. **2003**, *42*, 3009–3017.
[41] Zhang, X.; Qiao, X. F.; Shi, W.; Wu, J. B.; Jiang, D. S.; Tan, P. H. Phonon and Raman scattering of two-dimensional transition metal dichalcogenides from monolayer, multilayer to bulk material. *Chem. Soc. Rev*. **2015**, *44*, 2757–2785.
[42] Wu, J. B.; Lin, M. L.; Cong, X.; Liu, H. N.; Tan, P. H. Raman spectroscopy of graphene-based materials and its applications in related devices. *Chem. Soc. Rev*. **2018**, *47*, 1822–1873.
[43] Strong, V.; Dubin, S.; El-Kady, M. F.; Lech, A.; Wang, Y.; Weiller, B. H.; Kaner, R. B. Patterning and electronic tuning of laser scribed graphene for flexible all-carbon devices. *ACS Nano* **2012**, *6*, 1395–1403.
[44] Guo, L.; Jiang, H. B.; Shao, R. Q.; Zhang, Y. L.; Xie, S. Y.; Wang, J. N.; Li, X. B.; Jiang, F.; Chen, Q. D.; Zhang, T. et al. Two-beam-laser

interference mediated reduction, patterning and nanostructuring of graphene oxide for the production of a flexible humidity sensing device. *Carbon* **2012**, *50*, 1667–1673.

[45] Ning, J.; Hao, L.; Jin, M.; Qiu, X.; Shen, Y.; Liang, J.; Zhang, X.; Wang, B.; Li, X.; Zhi, L. A facile reduction method for roll-to-roll production of high performance graphene-based transparent conductive films. *Adv*. *Mater*. **2017**, *29*, 1605028.

[46] Qiao, H. Z.; Yang, J. J.; Wang, F.; Yang, Y.; Sun, J. L. Femtosecond laser direct writing of large-area two-dimensional metallic photonic crystal structures on tungsten surfaces. *Opt*. *Express* **2015**, *23*, 26617–26627.

[47] Liu, Z. M.; Siegel, J.; Garcia-Lechuga, M.; Epicier, T.; Lefkir, Y.; Reynaud, S.; Bugnet, M.; Vocanson, F.; Solis, J.; Vitrant, G. et al. Three-dimensional self-organization in nanocomposite layered systems by ultrafast laser pulses. *ACS Nano* **2017**, *11*, 5031–5040.

[48] Bricchi, E.; Klappauf, B. G.; Kazansky, P. G. Form birefringence and negative index change created by femtosecond direct writing in transparent materials. *Opt*. *Lett*. **2004**, *29*, 119–121.